ACS Energy LETTERS

http://pubs.acs.org/journal/aelccp

Extending the Electrochemical Window of Na^+ Halide Nanocomposite Solid Electrolytes for 5 V-Class All-Solid-State Na-Ion Batteries

Juhyoun Park,[⊥] Daseul Han,[⊥] Jun Pyo Son, Hiram Kwak, Wonseok Ko, Changhyun Park, Chanhee Lee, Hyun-Wook Lee, Jongsoon Kim, Kyung-Wan Nam,* and Yoon Seok Jung*

Cite This: *ACS Energy Lett.* 2024, 9, 2222−2230

Read Online

ACCESS | Metrics & More | Article Recommendations | Supporting Information

ABSTRACT: This study introduces a Na^+ fluorinated halide nanocomposite solid electrolyte (HNSE), ZrO_2-$2Na_2ZrCl_5F$, synthesized through a mechanochemical reaction using Na_2O. This HNSE exhibits a substantial improvement in Na^+ conductivity (2.1×10^{-5} S cm^{-1} at 30 °C) compared to Na_2ZrCl_5F (2.0×10^{-7} S cm^{-1}). The significant reduction in ionic conductivity of Na_2ZrCl_5F relative to Na_2ZrCl_6 (2.0×10^{-5} S cm^{-1}) is elucidated through synchrotron pair distribution function (PDF) analysis. Structural insights, including the fine structure of the ZrO_2 nanograins embedded in an amorphous Na_2ZrCl_5F matrix and the potential O-substituted interphase, are revealed through X-ray absorption spectroscopy, PDF, and cryogenic transmission electron microscopy. Fluorinated HNSEs offer exceptional electrochemical oxidative stability up to 5 V (vs Na/Na^+), enabling high-voltage cathode applications. $Na_{0.66}Ni_{0.1}Co_{0.1}Mn_{0.8}O_2$||$Na_3Sn$ all-solid-state cells using ZrO_2-$2Na_2ZrCl_5F$ as the catholyte demonstrate enhanced performance at 30 °C compared to cells using Na_2ZrCl_6 (47.4% capacity retention after 100 cycles vs 35.3% using Na_2ZrCl_6).

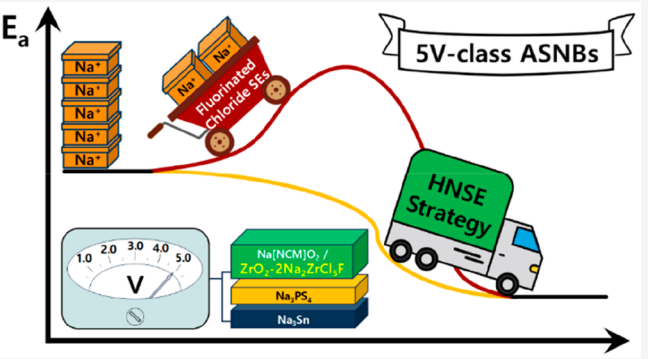

The expansion of lithium-ion batteries (LIBs) into large-scale applications, such as electric vehicles (kWh) and energy storage systems (>MWh),[1−3] is challenged by the unstable global supply chain of Li, which is exacerbated by environmental and political issues.[4−6] Safety concerns owing to flammable organic liquid electrolytes in LIBs further complicate their use.[7−10] All-solid-state Na-ion or Na batteries (ASNBs) with inorganic solid electrolytes (SEs) offer a promising alternative solution to these problems.[11−16]

Several types of inorganic Na^+ conducting SEs have been explored for ASNBs, including oxides (e.g., $Na_3Zr_2Si_2PO_{12}$, ~10^{-3} S cm^{-1}),[17] sulfides (e.g., Na_3PnS_4, Pn = P, Sb, max. ~10^{-2} S cm^{-1}),[11,18−23] halides (e.g., Na_2ZrCl_6, ~10^{-5} S cm^{-1}),[24,25] and closo-borates (e.g., $Na_2(B_{10}H_{10})_{0.5}(B_{12}H_{12})_{0.5}$, ~$10^{-3}$ S cm^{-1}).[26] Among these, halide SEs are notable candidates owing to the electrochemical oxidative stability of oxides and the mechanical deformability of sulfides.[24,25,27−35] Since the seminal report of trigonal Li_3YCl_6 and monoclinic Li_3YBr_6, which exhibited impressive Li^+ conductivities of 0.51 and 1.7 mS cm^{-1}, respectively,[27] the reignited investigation of halide SEs has resulted in the identification of novel compounds,[25,36] including the Li_xMCl_6 family (x = 2 or 3), such as Li_3YCl_6 (0.51 mS cm^{-1}),[27] Li_2ZrCl_6 (0.40 mS cm^{-1}),[31] Li_3YbCl_6 (0.14 mS cm^{-1}),[32] Li_3InCl_6 (1.49 mS cm^{-1}),[37] and Li_3ScCl_6 (3 mS cm^{-1}).[38]

In solid-state chemistry, elemental substitution is a common technique for controlling charge-carrier concentration or structural framework, which enhances the ionic conductivity of superionic conductors. This approach is effective for halide SEs, as demonstrated for various compounds, including $Li_{3-x}M_{1-x}Zr_xCl_6$ (M = Y, Er,[39] max. 1.4 mS cm^{-1}; M = In, Sc,[34] max. 2.1 mS cm^{-1}), $Li_{2+x}Zr_{1-x}M_xCl_6$ (M = Fe, Cr, V, max. 1.0 mS cm^{-1}),[31] and $Li_{3-x}Yb_{1-x}M_xCl_6$ (M = Zr, Hf, max. 1.5 mS cm^{-1}).[32] In addition, the choice of preparation methods, particularly mechanochemical preparation, significantly impacts the microstructures of halide SEs, particularly in terms of

Received: February 16, 2024
Revised: March 28, 2024
Accepted: April 8, 2024

https://doi.org/10.1021/acsenergylett.4c00490
ACS Energy Lett. 2024, 9, 2222−2230

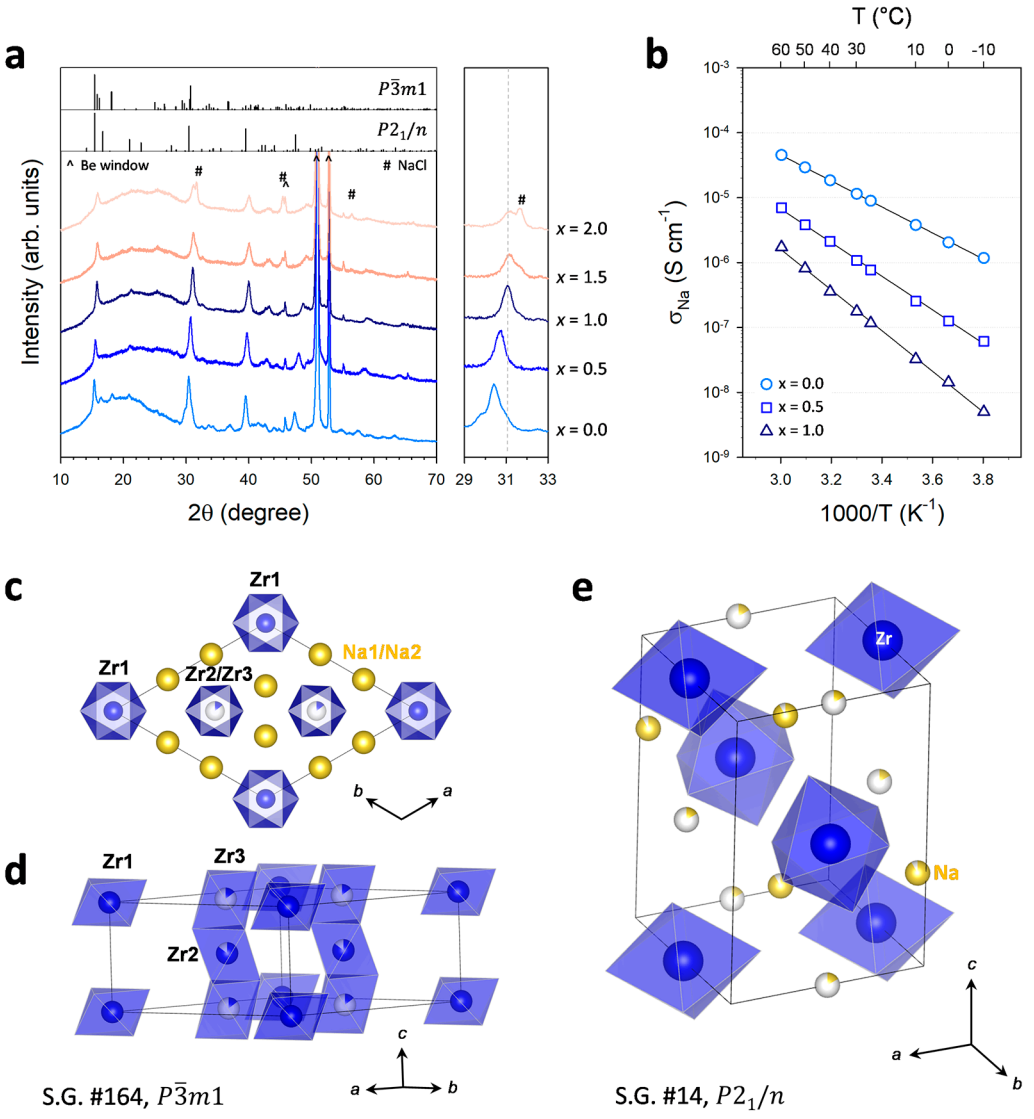

Figure 1. Characterization of fluorinated Na_2ZrCl_6 ($Na_2ZrCl_{6-x}F_x$). (a) XRD patterns and (b) Arrhenius plots of Na^+ conductivities of $Na_2ZrCl_{6-x}F_x$. Crystal structures of (c and d) $P\bar{3}m1$ and (e) $P2_1/n$.

structural disorder and metal distributions, which consequently affect their ionic conductivity.[40,41] While fewer Na^+ halide SEs have been identified compared to their Li^+ counterparts, their development has followed similar patterns.[25]

Na^+ halide SEs developed via composition tuning include $Na_{3-x}Er_{1-x}Zr_xCl_6$ (0.04 mS cm^{-1}),[42] $Na_{3-x}Y_{1-x}Zr_xCl_6$ (0.066 mS cm^{-1}),[43] $Na_{3-x}Yb_{1-x}Zr_xCl_6$ (0.066 mS cm^{-1}),[44] $Na_{3-x}Cr_{1-x}Zr_xCl_6$ (0.1 mS cm^{-1}),[45] and $Na_{3-x}In_{1-x}Zr_xCl_6$ (~0.01 mS cm^{-1}).[46] A significant enhancement in ionic conductivity has been observed in several compounds prepared using the mechanochemical method, such as Na_2ZrCl_6, $NaAlCl_4$, and Na_3InCl_6.[16,24,29,46,47] Specifically, ball-milled trigonal Na_2ZrCl_6 with a $P\bar{3}m1$ space group demonstrated a significant increase in ionic conductivity (1.8×10^{-5} S cm^{-1}) compared to its annealed counterpart (6.9×10^{-8} S cm^{-1}).[24] This difference in conductivity was presumed to stem from the occupation of an interstitial Na^+ site in the (002) plane, regulating Na^+ connectivity and thus the Na^+ migration energy landscape in the lattice. In a separate observation, the ball-milled sample exhibited both $P\bar{3}m1$ and $P2_1/n$ structures, unlike its annealed version, which exhibited only the $P\bar{3}m1$ structure.[47] The inclusion of the $P2_1/n$ structure in Na_2ZrCl_6 facilitates isotropic Na^+ migration pathways and intrinsic vacancies, leading to higher ionic conductivity.[47] For $NaAlCl_4$, a new Na site was identified in the mechanochemically prepared sample (3.9×10^{-6} S cm^{-1}), a feature absent in the annealed sample (3.3×10^{-7} S cm^{-1}).[16] This new site facilitates the formation of a net-like 2D ionic conduction pathway within the *ac*-plane. However, the advancement of halide-based ASNBs is often hindered by the limited ionic conductivities of several halide SEs, typically at approximately 10^{-5} S cm^{-1},[24,25,42,43,48] except for $NaAlCl_{4-2x}O_x$ (1.3 mS cm^{-1})[49] and Ta-based materials (2.7 and 4.6 mS cm^{-1} for $0.5Na_2O_2-TaCl_5$ and $x[Na_{0.75}(La/Sm)_{1.75}Cl_6]\cdot(1-x)$-$[NaTaCl_6]$, respectively).[50,51]

Our group recently demonstrated a novel method for ameliorating the ionic conductivity of halide SEs through interfacial conduction by using a nanocomposite strategy. Mechanochemical synthesis involving Li_2O or Na_2O has enabled the formation of partially O-substituted interphases

https://doi.org/10.1021/acsenergylett.4c00490
ACS Energy Lett. 2024, 9, 2222−2230

in halide nanocomposite SEs (HNSEs), significantly enhancing ionic conductivity from 0.40 to 1.3 mS cm^{-1} for Li HNSEs (ZrO_2-2LiCl-Li_2ZrCl_6) and from 0.011 to 0.11 mS cm^{-1} for Na HNSEs (0.13ZrO_2-0.61NaCl-0.26Na_2ZrCl_6).[29] However, the effectiveness of this strategy has yet to be investigated for fluorinated Na^+ halide SEs.

For practical applications, the prevalent use of rare and expensive central metals in halide SEs, such as Y, Sc, and In, poses a considerable challenge, with Al or Zr being the exceptions.[16,24,25,31] Recent theoretical and experimental investigations have emphasized the pivotal role of ternary (or quaternary) cations and halogen anions in determining the electrochemical stability of these SEs.[28] In particular, substituting Cl^- with F^- can extend the electrochemical oxidative limit. However, this advantage is offset by a decrease in the ionic conductivities. Moreover, the origins behind the decrease have not been clearly elucidated in relation to the crystal structure.[52] In the realm of Na^+ halide SEs, studies on enhancing the electrochemical stability of Na^+ chloride SEs are still lacking, specifically with the absence of cases for fluorinated Na^+ chloride SEs. Furthermore, while most previous studies on Na^+ halide SEs have focused on the 3 V-class $NaCrO_2$ cathode,[16,24,43] significant developments in various high-voltage Na^+ cathodes, such as $Na-Fe_{0.55}Mn_{0.44}Nb_{0.01}O_2$ (2.0−4.0 V) and $Na_{0.67}Mg_{0.22}Mn_{0.55}Fe_{0.23}O_2$ (2.0−4.5 V) also occurred.[53,54] Therefore, developing high-voltage halide Na^+ SEs to complement these cathode advancements is essential.

In this study, we present a new Na^+ halide SE comprising ZrO_2 and fluorinated Na_2ZrCl_5F nanograins, which significantly improved Na^+ conductivity (2.1×10^{-5} S cm^{-1} at 30 °C) compared to pure Na_2ZrCl_5F (2.0×10^{-7} S cm^{-1}). To the best of our knowledge, this is the first development of fluorinated Na^+ chloride SEs. The fluorinated HNSEs were synthesized via a mechanochemical reaction using Na_2O. Cryogenic scanning transmission electron microscopy (cryo-STEM) revealed nanostructures featuring ZrO_2 nanoparticles embedded within an amorphous Na_2ZrCl_5F matrix. Combined synchrotron X-ray pair distribution function (PDF) and X-ray absorption spectroscopy (XAS) comprehensively elucidated the fine structures of Na_2ZrCl_6 and Na_2ZrCl_5F, as well as the causes for the substantial decrease in Na^+ conductivity by fluorination, specifically from the perspective of the crystal structure. Furthermore, the ZrO_2−Na_2ZrCl_5F HNSE exhibited excellent electrochemical oxidative stability, reaching ∼5 V (vs Na/Na^+), rendering it suitable for high-voltage cathode applications. Its compatibility with a P2-type $Na_{0.66}Ni_{0.1}Co_{0.1}Mn_{0.8}O_2$ (NaNCM) in NaNCM||Na_3Sn ASNBs operating in 1.5−5.0 V at 30 °C was successfully demonstrated.

To explore the extent of fluorination in Na_2ZrCl_6, $Na_2ZrCl_{6-x}F_x$ samples with x = 0.0, 0.5, 1.0, 1.5, and 2.0 were prepared by using the mechanochemical method. The X-ray diffraction (XRD) patterns of these samples revealed that the original trigonal $P\bar{3}m1$ structure of Na_2ZrCl_6 is retained across all variants (Figure 1a).[24,43] Specifically, up to x = 1.0, a gradual positive shift in the (301) peak at ∼30.5° with no emerging impurity phases suggests a lattice contraction in Na_2ZrCl_6, which is attributed to the smaller ionic radius of F^- (133 pm) compared to that of Cl^- (181 pm).[55] However, at $x \geq 1.5$, the evolution of NaCl indicated a fluorination limit between x = 1.0 and 1.5.

The Na^+ conductivities of the cold-pressed pellets were measured by using the AC impedance method with Na^+-blocking Ti|SE|Ti symmetric cells. The corresponding Arrhenius plots for $Na_2ZrCl_{6-x}F_x$ (x = 0, 0.5, and 1.0) shown in Figure 1b indicate that fluorination substantially reduces the ionic conductivity of Na_2ZrCl_6, which is consistent with other fluorinated chloride compounds.[29,52] The ionic conductivity of Na_2ZrCl_6 at 30 °C was 1.1×10^{-5} S cm^{-1},[43] which decreased by 2 orders of magnitude to 2.0×10^{-7} S cm^{-1} upon fluorination (Na_2ZrCl_5F). The activation energy increased significantly from 0.398 to 0.605 eV. This substantially impeded Na^+ migration in fluorinated Na_2ZrCl_6 can be explained by a simple Coulombic force consideration (eq 1), which is a stronger Coulombic attraction between Na^+ and the anion framework.

$$|F| = k_e \frac{|q_1 q_2|}{r^2} \tag{1}$$

where k_e is the Coulombic constant, q_1 and q_2 are the magnitudes of the charges, and r is the distance between the charges.

The reduced lattice spacing due to fluorination implies a shorter distance between Na^+ and counteranions, resulting in stronger attractive forces that impede Na^+ migration in the channels.

Further, to deepen our understanding of the structure−transport relationship in fluorinated Na_2ZrCl_6, PDF curve fitting was performed on Na_2ZrCl_6 and Na_2ZrCl_5F in the range of 1.5−20 Å, as depicted in Figure S1. In addition, the structures calculated from the best-fit results are shown in Figure S2, and the corresponding structural information is tabulated in Table S1. Na_2ZrCl_6 was refined and revealed a composite structure, including the phases of $P\bar{3}m1$ and $P2_1/n$ structures (Figure 1c−e), which is consistent with a previous report.[42] Notably, the trigonal $P\bar{3}m1$ phase of Na_2ZrCl_6 exhibited higher site disorder in Zr^{4+} and Na^+ sites compared to Na_2ZrCl_5F (Figure S2), reflecting a controlled energy landscape that promotes enhanced Na^+ migration.[40] In contrast, Na_2ZrCl_5F was solely in the $P\bar{3}m1$ phase, without the inclusion of the $P2_1/n$ phase. Since the $P2_1/n$ phase has higher conductivity than $P\bar{3}m1$ because of intrinsic vacancies and isotropic conduction pathways,[47] the absence of the $P2_1/n$ phase in Na_2ZrCl_5F essentially contributes to its lower Na^+ conductivity. To pinpoint the specific sites of F^- and ascertain the occupation of Zr sites in Na_2ZrCl_5F, PDF fitting was conducted on symmetry-relaxed $P\bar{3}m1$ structures, focusing on whether Zr occupied the Zr2 or Zr3 sites. The fitting results reveal that F^- predominantly replaced the Cl sites in the $ZrCl_6$ polyhedra at the Zr2 and Zr3 sites, rather than those at the Zr1 site (Figure S2c,d). Notably, in Na_2ZrCl_5F, the Zr2 site occupancy is prevalent (72.9%) over the Zr3 site occupancy (24.9%). Additionally, the Na1 site (Wyckoff 6h) in the (002) plane exhibits a significantly high occupancy of 0.92 in the case of Zr2-occupied Na_2ZrCl_5F. These structural identifications explain the low ionic conductivity of Na_2ZrCl_5F, as the atomic arrangements with a lack of disorder in both metal and Na sites reflect inefficiency in Na^+ conduction within trigonal halide structure.[40] This is the first reported case demonstrating that metal site disorder influences the ionic conductivity in Na halide SEs. In summary, the 1/100 times decrease in Na^+ conductivity of Na_2ZrCl_5F compared to Na_2ZrCl_6 is attributed to the preferential Zr2 site occupation and site-ordering in the

https://doi.org/10.1021/acsenergylett.4c00490
ACS Energy Lett. 2024, 9, 2222−2230

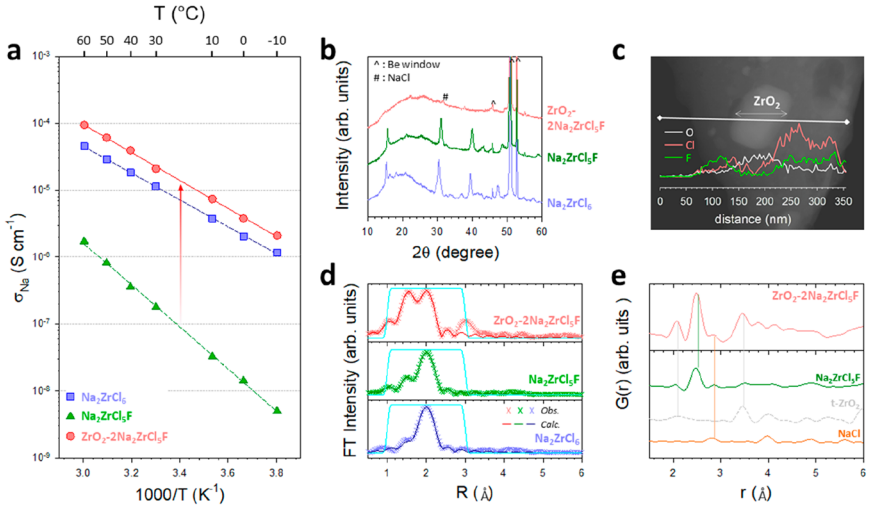

Figure 2. Characterization of ZrO_2-$2Na_2ZrCl_5F$ HNSE. (a) Arrhenius plots of ionic conductivities and (b) XRD patterns of ZrO_2-$2Na_2ZrCl_5F$ compared with conventional Na_2ZrCl_6 and Na_2ZrCl_5F. (c) STEM EDXS line maps for ZrO_2-$2Na_2ZrCl_5F$ HNSE. (d) EXAFS spectra of ZrO_2-$2Na_2ZrCl_5F$, Na_2ZrCl_5F, and Na_2ZrCl_6. (e) PDF $G(r)$ for ZrO_2-$2Na_2ZrCl_5F$, compared with references (Na_2ZrCl_5F, tetragonal ZrO_2 (t-ZrO_2), and NaCl).

ordered $P\bar{3}m1$ phase and the lack of a highly conductive $P2_1/n$ phase.

To enhance the ionic conductivity of Na_2ZrCl_5F, the HNSE strategy was applied, which involved the mechanochemical reaction of $ZrCl_4$ and ZrF_4 with Na_2O, as shown in eq 2.

$$4Na_2O + 5ZrCl_4 + ZrF_4 \rightarrow 2ZrO_2 + 4Na_2ZrCl_5F \quad (\approx ZrO_2\text{-}2Na_2ZrCl_5F) \tag{2}$$

Specifically, Na_2O reacts with $ZrCl_4$ (or ZrF_4) to form ZrO_2 nanoparticles alongside NaCl (or NaF). The remaining $ZrCl_4$ and ZrF_4 react with NaCl to yield Na_2ZrCl_5F. Figure 2a presents the Arrhenius plots, comparing the ionic conductivities of Na_2ZrCl_6, Na_2ZrCl_5F, and ZrO_2-$2Na_2ZrCl_5F$ HNSE. Nyquist plots of the ZrO_2-$2Na_2ZrCl_5F$ HNSE at various temperatures are shown in Figure S3. Notably, compared to Na_2ZrCl_5F, the Na^+ conductivity of the ZrO_2-$2Na_2ZrCl_5F$ HNSE demonstrated a substantial increase of 2 orders of magnitude, from 2.0×10^{-7} to 2.1×10^{-5} S cm^{-1}.

Furthermore, ZrO_2-NaCl-Na_2ZrCl_5F samples with varying ZrO_2 volume fractions of 0 to 7 vol % were prepared. Table S2 lists the Na^+ conductivities, recipes, and fractions of the samples. Fixed volume fractions of Na_2ZrCl_5F (93 vol %) were maintained, resulting in calculated ZrO_2 volume fractions in ZrO_2-$2Na_2ZrCl_5F$ and 0.29NaCl-0.71Na_2ZrCl_5F of 7 vol % and 0 vol %, respectively. The 0.29NaCl-0.71Na_2ZrCl_5F with the 7:93 (NaCl/Na_2ZrCl_5F) vol. ratio exhibited the lowest ionic conductivity of 9.5×10^{-7} S cm^{-1}. Although this value exceeded that of pure Na_2ZrCl_5F, the increase could be attributed to incomplete fluorination. Anion mixing between Cl in NaCl and F in Na_2ZrCl_5F, indicated by a shift in the XRD peak between Na_2ZrCl_6 and Na_2ZrCl_5F, supports this interpretation, as shown in Figure S4. In contrast, all the samples containing ZrO_2 (2.4, 4.9, and 7.0 vol %) exhibited high Na^+ conductivities exceeding 10^{-5} S cm^{-1}, verifying the pivotal role of the interphase between ZrO_2 and Na_2ZrCl_5F.

Figure 2b displays the XRD patterns of Na_2ZrCl_6, Na_2ZrCl_5F, and ZrO_2-$2Na_2ZrCl_5F$. The ZrO_2-$2Na_2ZrCl_5F$ HNSE exhibited no distinct peaks except for minor NaCl impurities, indicating poor crystallinity, nanograin formation, or amorphization owing to partial O-substitution.[29,49] The presence of ZrO_2 in the ZrO_2-$2Na_2ZrCl_5F$ HNSE was further confirmed through cryo-STEM energy-dispersive X-ray spectroscopy (EDXS) mapping, as depicted in Figures 2c and S5. Specifically, the matrix exhibited high concentrations of F and Cl around the nanoparticles along with high-intensity Zr and O signals within the nanoparticles, confirming the embedding of ZrO_2 nanoparticles in the Na_2ZrCl_5F matrix.

The local structure of the poorly crystalline ZrO_2-$2Na_2ZrCl_5F$ HNSE was further probed by using synchrotron XAS and PDF analyses. The Zr K-edge X-ray absorption near-edge structure (XANES) and extended X-ray absorption fine structure (EXAFS) spectra of ZrO_2-$2Na_2ZrCl_5F$ are plotted and compared with those of Na_2ZrCl_6 and Na_2ZrCl_5F in Figures S6 and 2d, respectively; the results are summarized in Table S3. The positions of the absorption edges between Na_2ZrCl_6 and ZrO_2 in the Zr K-edge XANES spectra confirmed the tetravalent oxidation state of Zr in both Na_2ZrCl_5F and ZrO_2-Na_2ZrCl_5F.[24,29,31] Notably, the absorption edges of Na_2ZrCl_5F and ZrO_2-$2Na_2ZrCl_5F$ shifted toward higher energies compared to those of Na_2ZrCl_6, signifying the presence of Zr−F and Zr−O bonds. Furthermore, an increase in the absorption edge intensity was observed for Na_2ZrCl_5F and ZrO_2-$2Na_2ZrCl_5F$ compared to Na_2ZrCl_6, which can be attributed to the presence of shorter Zr−O/F bonds and tetragonal-ZrO_2 (t-ZrO_2) with a higher coordination number. Typically, the pre-edge in XANES appears strong when the centrosymmetry collapses;[56] however, that of ZrO_2-$2Na_2ZrCl_5F$ does not intensify despite the formation of a t-ZrO_2 structure with distorted polyhedra. This might be due to the minimal energy difference between the 1s → *n*d and 1s → *n*p states in the Zr K-edge, in addition to a relatively small amount of the t-ZrO_2 phase compared to Na_2ZrCl_5F.[57] The appearance of the Zr−O peak at 1.5 Å in the EXAFS spectra (Figure 2d) verifies the formation of nanosized ZrO_2 in the ZrO_2-$2Na_2ZrCl_5F$ HNSE, corroborating the cryo-STEM results (Figures 2c and S5). The EXAFS fitting in the presence of t-ZrO_2 as a structural model resulted in a reasonable *R* value (1.3%), validating the presence of t-ZrO_2. Moreover, the Debye−Waller factor for ZrO_2-$2Na_2ZrCl_5F$ was higher than

https://doi.org/10.1021/acsenergylett.4c00490
ACS Energy Lett. 2024, 9, 2222−2230

those for both Na_2ZrCl_6 and Na_2ZrCl_5F, suggesting that ZrO_2-$2Na_2ZrCl_5F$ was either nanosized or amorphized (Table S3).

Figures 2e and S7 display the PDF results for ZrO_2-$2Na_2ZrCl_5F$ compared with those for Na_2ZrCl_6 and Na_2ZrCl_5F (Figures S1 and 2). Qualitative analysis up to 6 Å indicates that ZrO_2-$2Na_2ZrCl_5F$ exhibits distinct characteristics of both Na_2ZrCl_5F and t-ZrO_2, in addition to minor NaCl impurities (Figure 2e). The complex oscillations between 3 and 5 Å lead to speculation that ZrO_2-$2Na_2ZrCl_5F$ features a partially O-substituted interphase, consistent with the findings in our previous reported study.[29] Meanwhile, in cases where atomic arrangements lack consecutive sequences, PDF peaks tend to lose intensity across the entire *r*-range and eventually converge to 0.[58,59] Notably, for ZrO_2-$2Na_2ZrCl_5F$ (Figure S7), the PDF peaks exhibited rapid attenuation from significantly lower *r*-ranges compared to those of Na_2ZrCl_6 and Na_2ZrCl_5F. This suggests that the domains in ZrO_2-$2Na_2ZrCl_5F$ are significantly nanosized and lack structural coherence over long *r*-ranges, coinciding with the XRD and XAS results. Unfortunately, attempts to conduct a PDF fitting analysis for ZrO_2-$2Na_2ZrCl_5F$ to explore its long-range structural characteristics have been unsuccessful because of the lack of a model interphase structure.

The electrochemical stability of ZrO_2-$2Na_2ZrCl_5F$ HNSE was evaluated using cyclic voltammetry (CV) on an SE-C mixture electrode in $Na_3Sn|Na_3PS_4|$(SE-C) cells at 30 °C. Figures 3a and 3b show the first and second scan voltage

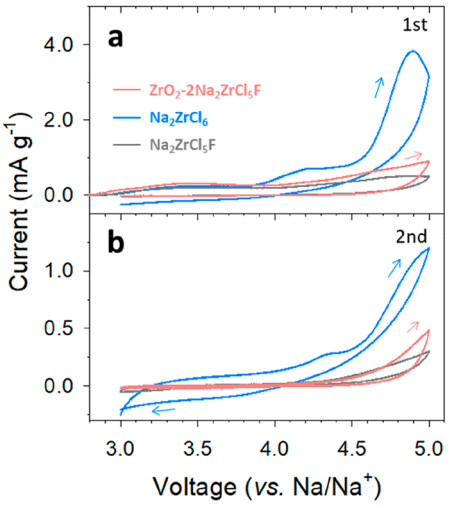

Figure 3. Cyclic voltammograms for $Na_3Sn|Na_3PS_4|$(SE-C) cells at 30 °C for ZrO_2-$2Na_2ZrCl_5F$ (red), Na_2ZrCl_5F (gray), and Na_2ZrCl_6 (blue). (a) First and (b) second CV profiles at 0.1 mV s^{-1}.

profiles of Na_2ZrCl_6, Na_2ZrCl_5F, and ZrO_2-$2Na_2ZrCl_5F$, respectively. Na_2ZrCl_6 exhibits a minor oxidative response up to 3.9 V (vs Na/Na^+), with an intense oxidation reaction initiating at 4.6 V (vs Na/Na^+). In contrast, Na_2ZrCl_5F and ZrO_2-$2Na_2ZrCl_5F$ demonstrate minor oxidation currents up to 5.0 V (vs Na/Na^+). In addition, the integrated oxidation currents up to 5.0 V (vs Na/Na^+) for Na_2ZrCl_5F and ZrO_2-$2Na_2ZrCl_5F$ are significantly lower (0.77 mA V g^{-1} for Na_2ZrCl_5F and 1.16 mA V g^{-1} for ZrO_2-$2Na_2ZrCl_5F$), compared to Na_2ZrCl_6 (2.52 mA V g^{-1}). Furthermore, Na_2ZrCl_6 exhibited cathodic signals that are particularly pronounced in the second negative scan, which is a characteristic absent in Na_2ZrCl_5F and ZrO_2-$2Na_2ZrCl_5F$, thus confirming their superior electrochemical stability compared to Na_2ZrCl_6 and highlighting the beneficial impact of fluorination.

To assess the effectiveness of ZrO_2-$2Na_2ZrCl_5F$ in 5 V-class ASNBs, we prepared (NaNCM-SE-C)$|Na_3PS_4|Na_3Sn$ all-solid-state cells and compared their performance with cells utilizing Na_2ZrCl_6 and Na_2ZrCl_5F at 30 °C. The cells were charged at 0.1 C (0.12 mA cm^{-2}) with a constant current−constant voltage mode (CCCV, a limiting current of 0.012 mA cm^{-2}) and discharged at 0.1 C between 1.5 and 5.0 V (vs Na/Na^+). The results are presented in Figure 4 and Table S4. The

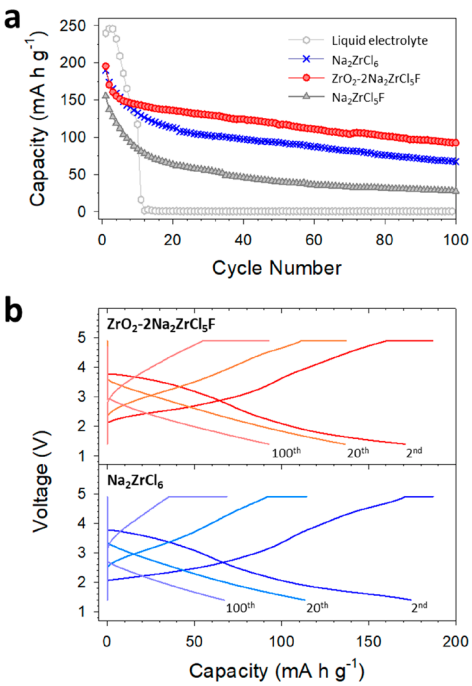

Figure 4. Electrochemical performance of $Na_3Sn|Na_{0.66}Ni_{0.1}Co_{0.1}Mn_{0.8}O_2$ all-solid-state Na^+ batteries (ASNBs) employing ZrO_2-$2Na_2ZrCl_5F$, Na_2ZrCl_5F, and Na_2ZrCl_6 at 0.1C and 30 °C. (a) Cycling performance and (b) corresponding charge−discharge voltage profiles. Voltage profiles and Coulombic efficiency of cells are displayed in Figures S8−S11.

cycling performance and corresponding charge−discharge voltage profiles at different cycles are presented in Figure 4a,b. Notably, the NaNCM||Na half-cell with a commercial liquid electrolyte (1 M $NaPF_6$ in a 97:3 volume ratio mixture of propylene carbonate and fluoroethylene carbonate) exhibits poor reversibility (Figures 4a and S8). In contrast, ASNBs with halide SEs demonstrated relatively decent reversibility despite gradual capacity fading, which can be ascribed to (i) interfacial electrochemical and (electro)chemomechanical degradation and (ii) the degradation of bulk NaNCM. For NaNCM, a structural transition involving P′2 phase formation and vacancy ordering contributes to capacity fading when operated between 1.5 and 5.0 V (vs Na/Na^+).[60,61] The ASNB cells demonstrated high initial discharge capacities of 196 and 190 mA h g^{-1} for ZrO_2-$2Na_2ZrCl_5F$ and Na_2ZrCl_6, respectively. These comparable values correlate with their similar Na^+ conductivities (2.1×10^{-5} and 1.1×10^{-5} S cm^{-1} for ZrO_2-$2Na_2ZrCl_5F$ and Na_2ZrCl_6, respectively). However, ZrO_2-$2Na_2ZrCl_5F$ demonstrated a higher capacity retention than Na_2ZrCl_6. Although

https://doi.org/10.1021/acsenergylett.4c00490
ACS Energy Lett. 2024, 9, 2222−2230

the initial discharge capacities and capacity fading (from the second to fifth cycles) were comparable for both, the capacity fading for ZrO_2-$2Na_2ZrCl_5F$ was mitigated after the sixth cycle, in contrast to the continuous fading observed for Na_2ZrCl_6. Concurrently, the overpotential in the charge−discharge profile of Na_2ZrCl_6 exceeded that of ZrO_2-$2Na_2ZrCl_5F$ after the 20th cycle (Figure S9), indicating that the interfacial stability effect became more pronounced. The superior cycling stability of ZrO_2-$2Na_2ZrCl_5F$ suggests a more stable nature and faster formation of passivating interfaces compared to Na_2ZrCl_6.[29,50] Consistently, ZrO_2-$2Na_2ZrCl_5F$ demonstrated superior Coulombic efficiencies, averaging 97.93% from the second to the 20th cycles vs 97.36% for Na_2ZrCl_6 (Figure S10).

However, despite the CV results confirming the superior oxidative stability of Na_2ZrCl_5F over Na_2ZrCl_6 (Figure 3), the observed poorer cycle retention and Coulombic efficiency for Na_2ZrCl_5F, as compared to Na_2ZrCl_6, are noteworthy (Figures 4a and S10). This discrepancy can be attributed to the cycling test protocol, specifically the CCCV charging mode. The significantly lower ionic conductivity of Na_2ZrCl_5F (2.0×10^{-7} S cm^{-1}) compared to Na_2ZrCl_6 (1.1×10^{-5} S cm^{-1}) or ZrO_2-$2Na_2ZrCl_5F$ (2.1×10^{-5} S cm^{-1}) led to the cells employing Na_2ZrCl_5F spending considerably more time at the constant voltage of 5.0 V (vs Na/Na$^+$), as found in Figure S11. For example, during the first charging phase, the period spent at constant voltage was 420 min for Na_2ZrCl_5F, much longer than 215 min for Na_2ZrCl_6 or 238 min for ZrO_2-$2Na_2ZrCl_5F$. This extended duration at high voltage exacerbated side reactions, thereby leading to capacity fading. These findings suggest the limitation of solely relying on fluorination to achieve the desired high-voltage stability of as high as 5 V (vs Na/Na$^+$) and emphasize the necessity of addressing the compromised ionic conductivity caused by fluorination through the HNSE strategy.

To quantify the cathode−SE interfacial stability in NaNCM|Na_3PS_4|Na_3Sn cells, electrochemical impedance spectroscopy (EIS) analyses were conducted, and the results are summarized in Figure 5a,b. In the Nyquist plots (Figure 5a), an incomplete high-frequency semicircle and a full midfrequency semicircle are observed, representing the resistances of the Na_3PS_4 separating layer and the cathode−halide SE interfaces, respectively.[16,24,31,62] The results fitted with the equivalent circuit model (Figure S12) are displayed in Figure 5b and listed in Table S5. The comparable $R_1 + R_2$ amplitudes for both cells (approximately 1200−1600 Ω) are attributed to the use of identical Na_3PS_4 SE layers. In the second cycle, the cell with Na_2ZrCl_6 exhibited a lower R_3 value (42.2 Ω) compared to the ZrO_2-$2Na_2ZrCl_5F$ cell (122.6 Ω), despite the latter's slightly higher ionic conductivity (2.1×10^{-5} vs 1.1×10^{-5} S cm^{-1}). This discrepancy is likely due to the contact hindrance with NaNCM particles caused by ZrO_2 in the HNSE particles.[26] Notably, the R_3 value of Na_2ZrCl_6 exceeded that of ZrO_2-$2Na_2ZrCl_5F$ after the 5th to 10th cycles, culminating in a substantially larger value at the 20th cycle: 947 vs 1461 Ω. This trend aligns well with the cycling performance behavior observed in Figures 4, S9, and S10.

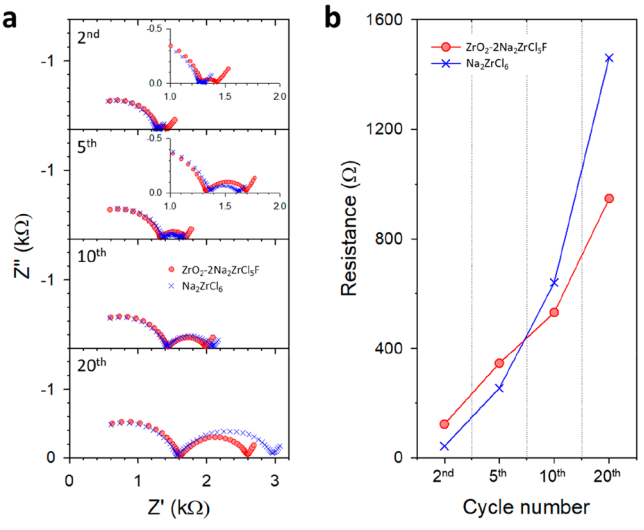

Figure 5. EIS results of Na_3Sn|$Na_{0.66}Ni_{0.1}Co_{0.1}Mn_{0.8}O_2$ ASNB cells employing Na_2ZrCl_6 or ZrO_2-$2Na_2ZrCl_5F$ HNSE at 30 °C. (a) Nyquist plots at 2nd, 5th, 10th, and 20th cycles. (b) Fitted resistance as a function of cycle number.

In summary, the newly developed Na$^+$-conducting fluorinated HNSE ZrO_2-$2Na_2ZrCl_5F$ was synthesized using a mechanochemical method and demonstrated an Na$^+$ conductivity of 2.1×10^{-5} S cm^{-1} at 30 °C. HNSEs comprising ZrO_2 nanoparticles embedded in an amorphous Na_2ZrCl_5F matrix with the evolution of a potential O-substituted interphase were formed by reacting Na_2O with the metal halide precursors—$ZrCl_4$ and ZrF_4. The HNSE nanostructures were confirmed through synergistic structural analyses, which included synchrotron XAS, PDF, and cryo-STEM. Fluorination in Na_2ZrCl_6 led to a significant decrease in ionic conductivity from 1.1×10^{-5} to 2.0×10^{-7} S cm^{-1} in Na_2ZrCl_5F. Synchrotron PDF analysis revealed the underlying mechanism, which was characterized by the higher occupation of the Zr2-site over the Zr3-site in the $P\bar{3}m1$ structure and the absence of a highly conductive $P2_1/n$ phase. However, by implementing an interfacial conduction strategy in the HNSEs, the Na$^+$ conductivity of Na_2ZrCl_5F increased by approximately 2 orders of magnitude. This improvement was attributed to enhanced interfacial Na$^+$ transport in the ZrO_2-$2Na_2ZrCl_5F$ nanostructures. The electrochemical oxidative stability of ZrO_2-$2Na_2ZrCl_5F$ was significantly enhanced, exhibiting stability up to 5 V (vs Na/Na$^+$), as evidenced by the CV results. The efficacy of ZrO_2-$2Na_2ZrCl_5F$ in enabling 5 V-class cathode NaNCM in ASNBs was successfully demonstrated. Our results provide invaluable insights into the design of high-voltage superionic conductors and contribute to advancing the field of high-performance all-solid-state batteries.

■ ASSOCIATED CONTENT

Supporting Information

The Supporting Information is available free of charge at https://pubs.acs.org/doi/10.1021/acsenergylett.4c00490.

Experimental methods, PDF refinement profiles, crystal structures of Na_2ZrCl_6 and Na_2ZrCl_5F with $P\bar{3}m1$ and $P2_1/n$ space groups, results of ZrO_2−NaCl−Na_2ZrCl_5F HNSEs with fixed volume fraction of Na_2ZrCl_5F (Nyquist Plots, Arrhenius plots, Na$^+$ conductivity, activation energy, and XRD profiles), STEM EDXS images, XANES spectra, electrochemical performances of liquid electrolyte cells and ASNB cells using NaNCM, equivalent circuit, detailed characteristics of HNSEs, EXAFS fitting results, and fitted EIS results (PDF)

https://doi.org/10.1021/acsenergylett.4c00490
ACS Energy Lett. 2024, 9, 2222−2230

AUTHOR INFORMATION

Corresponding Authors

Kyung-Wan Nam − *Department of Energy and Materials Engineering, Dongguk University, Seoul 04620, South Korea*; orcid.org/0000-0001-6278-6369; Email: knam@dongguk.edu

Yoon Seok Jung − *Department of Chemical and Biomolecular Engineering, Yonsei University, Seoul 03722, South Korea*; Email: yoonsjung@yonsei.ac.kr

Authors

Juhyoun Park − *Department of Chemical and Biomolecular Engineering, Yonsei University, Seoul 03722, South Korea*

Daseul Han − *Department of Energy and Materials Engineering, Dongguk University, Seoul 04620, South Korea*

Jun Pyo Son − *Department of Chemical and Biomolecular Engineering, Yonsei University, Seoul 03722, South Korea*

Hiram Kwak − *Department of Chemical and Biomolecular Engineering, Yonsei University, Seoul 03722, South Korea*

Wonseok Ko − *Department of Energy Science, Sungkyunkwan University (SKKU), Suwon 440-746, South Korea; SKKU Institute of Energy Science and Technology (SIEST), Sungkyunkwan University, Suwon 16419, South Korea*

Changhyun Park − *School of Energy and Chemical Engineering, Ulsan National Institute of Science and Technology (UNIST), Ulsan 44919, South Korea*

Chanhee Lee − *School of Energy and Chemical Engineering, Ulsan National Institute of Science and Technology (UNIST), Ulsan 44919, South Korea*

Hyun-Wook Lee − *School of Energy and Chemical Engineering, Ulsan National Institute of Science and Technology (UNIST), Ulsan 44919, South Korea*; orcid.org/0000-0001-9074-1619

Jongsoon Kim − *Department of Energy Science, Sungkyunkwan University (SKKU), Suwon 440-746, South Korea; SKKU Institute of Energy Science and Technology (SIEST), Sungkyunkwan University, Suwon 16419, South Korea*

Complete contact information is available at: https://pubs.acs.org/10.1021/acsenergylett.4c00490

Author Contributions

⊥J.P. and D.H. contributed equally.

Notes

The authors declare no competing financial interest.

ACKNOWLEDGMENTS

This work was supported by the Samsung Science and Technology Foundation under project no. SRFC-MA2102-03 and by the National Research Foundation of Korea (NRF), funded by the Ministry of Science, ICT & Future Planning (2022M3J1A1085397). The PDF research used beamline 28-ID-1 (PDF) of the National Synchrotron Light Source II, a US Department of Energy (DOE) Office of Science User Facility operated for the DOE Office of Science by Brookhaven National Laboratory under contract no. DE-SC0012704. Y.S.J. is grateful to Prof. Dong-Hwa Seo and Jae-Seung Kim at KAIST for fruitful discussions.

REFERENCES

(1) Hannan, M.; Hoque, M. M.; Mohamed, A.; Ayob, A. Review of energy storage systems for electric vehicle applications: Issues and challenges. *Renew. & Sus. Energy Rev.* **2017**, *69*, 771−789.

(2) Goodenough, J. B.; Kim, Y. Challenges for rechargeable Li batteries. *Chem. Mater.* **2010**, *22*, 587−603.

(3) Dunn, B.; Kamath, H.; Tarascon, J.-M. Electrical energy storage for the grid: a battery of choices. *Science* **2011**, *334*, 928−935.

(4) Hwang, J.-Y.; Myung, S.-T.; Sun, Y.-K. Sodium-ion batteries: present and future. *Chem. Soc. Rev.* **2017**, *46*, 3529−3614.

(5) Abraham, K. M. How comparable are sodium-ion batteries to lithium-ion counterparts? *ACS Energy Lett.* **2020**, *5*, 3544−3547.

(6) Fleischmann, J.; Hanike, M.; Horetsky, E.; Ibrahim, D.; Jautelat, S.; Linder, M.; Schaufuss, P.; Torscht, L.; van de Rijt, A. *Battery 2030: Resilient, sustainable, and circula*; Mckinsey & Company, 2023; pp 218

(7) Wang, J.; Yamada, Y.; Sodeyama, K.; Watanabe, E.; Takada, K.; Tateyama, Y.; Yamada, A. Fire-extinguishing organic electrolytes for safe batteries. *Nat. Energy* **2018**, *3*, 22−29.

(8) Liu, K.; Liu, Y.; Lin, D.; Pei, A.; Cui, Y. Materials for lithium-ion battery safety. *Sci. Adv.* **2018**, *4*, No. eaas9820.

(9) Liu, Y. K.; Zhao, C. Z.; Du, Z.; Zhang, X. Q.; Chen, A. B.; Zhang, Q. Research Progresses of Liquid Electrolytes in Lithium-Ion Batteries. *Small* **2023**, *19*, 2205315.

(10) Stephenson, T.; Li, Z.; Olsen, B.; Mitlin, D. Lithium ion battery applications of molybdenum disulfide (MoS_2) nanocomposites. *Energy Environ. Sci.* **2014**, *7*, 209−231.

(11) Banerjee, A.; Park, K. H.; Heo, J. W.; Nam, Y. J.; Moon, C. K.; Oh, S. M.; Hong, S. T.; Jung, Y. S. Na_3SbS_4: a solution processable sodium superionic conductor for all-solid-state sodium-ion batteries. *Angew. Chem., Int. Ed.* **2016**, *128*, 9786−9790.

(12) Duchêne, L.; Kühnel, R.-S.; Stilp, E.; Reyes, E. C.; Remhof, A.; Hagemann, H.; Battaglia, C. A stable 3 V all-solid-state sodium-ion battery based on a closo-borate electrolyte. *Energy Environ. Sci.* **2017**, *10*, 2609−2615.

(13) Kim, J. J.; Yoon, K.; Park, I.; Kang, K. Progress in the development of sodium-ion solid electrolytes. *Small Methods* **2017**, *1*, 1700219.

(14) Zhao, C.; Liu, L.; Qi, X.; Lu, Y.; Wu, F.; Zhao, J.; Yu, Y.; Hu, Y. S.; Chen, L. Solid-state sodium batteries. *Adv. Energy Mater.* **2018**, *8*, 1703012.

(15) Lu, Y.; Li, L.; Zhang, Q.; Niu, Z.; Chen, J. Electrolyte and interface engineering for solid-state sodium batteries. *Joule* **2018**, *2*, 1747−1770.

(16) Park, J.; Son, J. P.; Ko, W.; Kim, J.-S.; Choi, Y.; Kim, H.; Kwak, H.; Seo, D.-H.; Kim, J.; Jung, Y. S. $NaAlCl_4$: New Halide Solid Electrolyte for 3 V Stable Cost-Effective All-Solid-State Na-Ion Batteries. *ACS Energy Lett.* **2022**, *7*, 3293−3301.

(17) Chen, S.; Wu, C.; Shen, L.; Zhu, C.; Huang, Y.; Xi, K.; Maier, J.; Yu, Y. Challenges and perspectives for NASICON-type electrode materials for advanced sodium-ion batteries. *Adv. Mater.* **2017**, *29*, 1700431.

(18) Hayashi, A.; Noi, K.; Sakuda, A.; Tatsumisago, M. Superionic glass-ceramic electrolytes for room-temperature rechargeable sodium batteries. *Nat. Commun.* **2012**, *3*, 856.

(19) Chen, S.; Xie, D.; Liu, G.; Mwizerwa, J. P.; Zhang, Q.; Zhao, Y.; Xu, X.; Yao, X. Sulfide solid electrolytes for all-solid-state lithium batteries: Structure, conductivity, stability and application. *Energy Storage Mater.* **2018**, *14*, 58−74.

(20) Fuchs, T.; Culver, S. P.; Till, P.; Zeier, W. G. Defect-mediated conductivity enhancements in $Na_{3-x}Pn_{1-x}W_xS_4$ (Pn = P, Sb) using aliovalent substitutions. *ACS Energy Lett.* **2020**, *5*, 146−151.

(21) Wu, J.; Liu, S.; Han, F.; Yao, X.; Wang, C. Lithium/sulfide all-solid-state batteries using sulfide electrolytes. *Adv. Mater.* **2021**, *33*, 2000751.

(22) Zhang, Q.; Cao, D.; Ma, Y.; Natan, A.; Aurora, P.; Zhu, H. Sulfide-based solid-state electrolytes: synthesis, stability, and potential for all-solid-state batteries. *Adv. Mater.* **2019**, *31*, 1901131.

(23) Zhang, Q.; Zhang, C.; Hood, Z. D.; Chi, M.; Liang, C.; Jalarvo, N. H.; Yu, M.; Wang, H. Abnormally low activation energy in cubic Na_3SbS_4 superionic conductors. *Chem. Mater.* **2020**, *32*, 2264−2271.
(24) Kwak, H.; Lyoo, J.; Park, J.; Han, Y.; Asakura, R.; Remhof, A.; Battaglia, C.; Kim, H.; Hong, S.-T.; Jung, Y. S. Na_2ZrCl_6 enabling highly stable 3 V all-solid-state Na-ion batteries. *Energy Storage Mater.* **2021**, *37*, 47−54.
(25) Kwak, H.; Wang, S.; Park, J.; Liu, Y.; Kim, K. T.; Choi, Y.; Mo, Y.; Jung, Y. S. Emerging Halide Superionic Conductors for All-Solid-State Batteries: Design, Synthesis, and Practical Applications. *ACS Energy Lett.* **2022**, *7*, 1776−1805.
(26) Duchêne, L.; Remhof, A.; Hagemann, H.; Battaglia, C. Status and prospects of hydroborate electrolytes for all-solid-state batteries. *Energy Storage Mater.* **2020**, *25*, 782−794.
(27) Asano, T.; Sakai, A.; Ouchi, S.; Sakaida, M.; Miyazaki, A.; Hasegawa, S. Solid halide electrolytes with high lithium-ion conductivity for application in 4 V class bulk-type all-solid-state batteries. *Adv. Mater.* **2018**, *30*, 1803075.
(28) Wang, S.; Bai, Q.; Nolan, A. M.; Liu, Y.; Gong, S.; Sun, Q.; Mo, Y. Lithium chlorides and bromides as promising solid-state chemistries for fast ion conductors with good electrochemical stability. *Angew. Chem., Int. Ed.* **2019**, *58*, 8039−8043.
(29) Kwak, H.; Kim, J.-S.; Han, D.; Kim, J. S.; Park, J.; Kwon, G.; Bak, S.-M.; Heo, U.; Park, C.; Lee, H.-W.; Nam, K. W.; Seo, D. H.; Jung, Y. S. Boosting the interfacial superionic conduction of halide solid electrolytes for all-solid-state batteries. *Nat. Commun.* **2023**, *14*, 2459.
(30) Liu, Z.; Ma, S.; Liu, J.; Xiong, S.; Ma, Y.; Chen, H. High ionic conductivity achieved in $Li_3Y(Br_3Cl_3)$ mixed halide solid electrolyte via promoted diffusion pathways and enhanced grain boundary. *ACS Energy Lett.* **2021**, *6*, 298−304.
(31) Kwak, H.; Han, D.; Lyoo, J.; Park, J.; Jung, S. H.; Han, Y.; Kwon, G.; Kim, H.; Hong, S. T.; Nam, K. W.; Jung, Y. S. New Cost-Effective Halide Solid Electrolytes for All-Solid-State Batteries: Mechanochemically Prepared Fe^{3+}-Substituted Li_2ZrCl_6. *Adv. Energy Mater.* **2021**, *11*, 2003190.
(32) Park, J.; Han, D.; Kwak, H.; Han, Y.; Choi, Y. J.; Nam, K.-W.; Jung, Y. S. Heat treatment protocol for modulating ionic conductivity via structural evolution of $Li_{3-x}Yb_{1-x}M_xCl_6$ (M = Hf^{4+}, Zr^{4+}) new halide superionic conductors for all-solid-state batteries. *Chem. Eng. J.* **2021**, *425*, 130630.
(33) Kim, K.; Park, D.; Jung, H.-G.; Chung, K. Y.; Shim, J. H.; Wood, B. C.; Yu, S. Material design strategy for halide solid electrolytes Li_3MX_6 (X= Cl, Br, and I) for all-solid-state high-voltage Li-ion batteries. *Chem. Mater.* **2021**, *33*, 3669−3677.
(34) Kwak, H.; Han, D.; Son, J. P.; Kim, J. S.; Park, J.; Nam, K.-W.; Kim, H.; Jung, Y. S. Li^+ conduction in aliovalent-substituted monoclinic Li_2ZrCl_6 for all-solid-state batteries: $Li_{2+x}Zr_{1-x}M_xCl_6$ (M= In, Sc). *Chem. Eng. J.* **2022**, *437*, 135413.
(35) Kim, J. S.; Jung, S.; Kwak, H.; Han, Y.; Kim, S.; Lim, J.; Lee, Y. M.; Jung, Y. S. Synergistic halide-sulfide hybrid solid electrolytes for Ni-rich cathodes design guided by digital twin for all-solid-State Li batteries. *Energy Storage Mater.* **2023**, *55*, 193−204.
(36) Li, X.; Liang, J.; Yang, X.; Adair, K. R.; Wang, C.; Zhao, F.; Sun, X. Progress and perspectives on halide lithium conductors for all-solid-state lithium batteries. *Energy Environ. Sci.* **2020**, *13*, 1429−1461.
(37) Liang, J.; Li, X.; Wang, S.; Adair, K. R.; Li, W.; Zhao, Y.; Wang, C.; Hu, Y.; Zhang, L.; Zhao, S.; Lu, S.; Huang, H.; Li, R.; Mo, Y.; Sun, X. Site-Occupation-Tuned Superionic Li_xScCl_{3+x} Halide Solid Electrolytes for All-Solid-State Batteries. *J. Am. Chem. Soc.* **2020**, *142*, 7012−7022.
(38) Li, X.; Liang, J.; Luo, J.; Norouzi Banis, M.; Wang, C.; Li, W.; Deng, S.; Yu, C.; Zhao, F.; Hu, Y.; Sham, T.-K.; Zhang, L.; Zhao, S.; Lu, S.; Huang, H.; Li, R.; Adair, K. R.; Sun, X. Air-stable Li_3InCl_6 electrolyte with high voltage compatibility for all-solid-state batteries. *Energy Environ. Sci.* **2019**, *12*, 2665−2671.
(39) Park, K.-H.; Kaup, K.; Assoud, A.; Zhang, Q.; Wu, X.; Nazar, L. F. High-voltage superionic halide solid electrolytes for all-solid-state Li-ion batteries. *ACS Energy Lett.* **2020**, *5*, 533−539.
(40) Schlem, R.; Muy, S.; Prinz, N.; Banik, A.; Shao-Horn, Y.; Zobel, M.; Zeier, W. G. Mechanochemical synthesis: a tool to tune cation site disorder and ionic transport properties of Li_3MCl_6 (M= Y, Er) superionic conductors. *Adv. Energy Mater.* **2020**, *10*, 1903719.
(41) Sebti, E.; Evans, H. A.; Chen, H.; Richardson, P. M.; White, K. M.; Giovine, R.; Koirala, K. P.; Xu, Y.; Gonzalez-Correa, E.; Wang, C.; Brown, C. M.; Cheetham, A. K.; Canepa, P.; Clément, R. J. Stacking faults assist lithium-ion conduction in a halide-based superionic conductor. *J. Am. Chem. Soc.* **2022**, *144*, 5795−5811.
(42) Schlem, R.; Banik, A.; Eckardt, M.; Zobel, M.; Zeier, W. G. $Na_{3-x}Er_{1-x}Zr_xCl_6$—A Halide-Based Fast Sodium-Ion Conductor with Vacancy-Driven Ionic Transport. *ACS Appl. Energy Mater.* **2020**, *3*, 10164−10173.
(43) Wu, E. A.; Banerjee, S.; Tang, H.; Richardson, P. M.; Doux, J.-M.; Qi, J.; Zhu, Z.; Grenier, A.; Li, Y.; Zhao, E.; Deysher, G.; Sebti, E.; Nguyen, H.; Stephens, R.; Verbist, G.; Chapman, K. W.; Clément, R. J.; Banerjee, A.; Meng, Y. S.; Ong, S. P. A stable cathode-solid electrolyte composite for high-voltage, long-cycle-life solid-state sodium-ion batteries. *Nat. Commun.* **2021**, *12*, 1256.
(44) Li, L.; Yao, J.; Xu, R.; Lin, Q.; Yan, X.; Yu, C.; Zhang, L. Highly stable and encapsulation-microstructrual cathode derived by self-pressurization behavior in Na-halides-based all-solid-state batteries. *Energy Storage Mater.* **2023**, *63*, 103016.
(45) Wang, L.; Song, Z.; Lou, X.; Chen, Y.; Wang, T.; Wang, Z.; Chen, H.; Yin, W.; Avdeev, M.; Kan, W. H.; Hu, B.; Luo, W. $Na_{2.5}Cr_{0.5}Zr_{0.5}Cl_6$: A New Halide-Based Fast Sodium-Ion Conductor. *Small* **2024**, 2400195.
(46) Okada, Y.; Kimura, T.; Motohashi, K.; Sakuda, A.; Hayashi, A. Mechanochemical Synthesis and Characterization of $Na_{3-x}In_{1-x}Zr_xCl_6$ Solid Electrolyte. *Electrochemistry* **2023**, *91*, 077009−077009.
(47) Sebti, E.; Qi, J.; Richardson, P. M.; Ridley, P.; Wu, E. A.; Banerjee, S.; Giovine, R.; Cronk, A.; Ham, S.-Y.; Meng, Y. S.; Clément, R. J. Synthetic control of structure and conduction properties in Na-Y-Zr-Cl solid electrolytes. *J. Mater. Chem. A* **2022**, *10*, 21565−21578.
(48) Meyer, G.; Peter Ax, S.; Schleid, T.; Irmler, M. The chlorides Na_3MCl_6 (M = Eu-Lu, Y, Sc): Synthesis, crystal structures, and thermal behaviour. *Z. Anorg. Allg. Chem.* **1987**, *554*, 25−33.
(49) Dai, T.; Wu, S.; Lu, Y.; Yang, Y.; Liu, Y.; Chang, C.; Rong, X.; Xiao, R.; Zhao, J.; Liu, Y.; Wang, W.; Chen, L.; Hu, Y. S. Inorganic glass electrolytes with polymer-like viscoelasticity. *Nat. Energy* **2023**, *8*, 1221−1228.
(50) Fu, J.; Wang, S.; Wu, D.; Luo, J.; Wang, C.; Liang, J.; Lin, X.; Hu, Y.; Zhang, S.; Zhao, F.; Li, W.; Li, M.; Duan, H.; Zhao, Y.; Gu, M.; Sham, T.-K.; Mo, Y.; Sun, X. Halide Heterogeneous Structure Boosting Ionic Diffusion and High-Voltage Stability of Sodium Superionic Conductors. *Adv. Mater.* **2024**, *36*, 2308012.
(51) Lin, X.; Zhao, Y.; Wang, C.; Luo, J.; Fu, J.; Xiao, B.; Gao, Y.; Li, W.; Zhang, S.; Xu, J.; Yang, F.; Hao, X.; Duan, H.; Sun, Y.; Guo, J.; Huang, Y.; Sun, X. A Dual Anion Chemistry-Based Superionic Glass Enabling Long-Cycling All-Solid-State Sodium-Ion Batteries. *Angew. Chem., Int. Ed.* **2024**, *63*, e202314181.
(52) Zhang, S.; Zhao, F.; Wang, S.; Liang, J.; Wang, J.; Wang, C.; Zhang, H.; Adair, K.; Li, W.; Li, M.; Duan, H.; Zhao, Y.; Yu, R.; Li, R.; Huang, H.; Zhang, L.; Zhao, S.; Lu, S.; Sham, T.-K.; Mo, Y.; Sun, X. Advanced High-Voltage All-Solid-State Li-Ion Batteries Enabled by a Dual-Halogen Solid Electrolyte. *Adv. Energy Mater.* **2021**, *11*, 2100836.
(53) Zhang, L.; Yuan, T.; Soule, L.; Sun, H.; Pang, Y.; Yang, J.; Zheng, S. Enhanced Ionic Transport and Structural Stability of Nb-Doped O3-$NaFe_{0.55}Mn_{0.45-x}Nb_xO_2$ Cathode Material for Long-Lasting Sodium-Ion Batteries. *ACS Appl. Energy Mater.* **2020**, *3*, 3770−3778.
(54) Lee, S.; Ko, W.; Park, H.; Lee, Y.; Kang, J.; Ahn, J.; Lee, S.; Sim, E.; Ihm, K.; Park, K.-Y.; Kim, J. Gradational anionic redox enabling high-energy P2-type Na-layered oxide cathode. *Chem. Eng. J.* **2023**, *451*, 138883.
(55) Shannon, R. D. Revised effective ionic radii and systematic studies of interatomic distances in halides and chalcogenides. *Acta*

Crystallogr. A: Cryst. Phys. Diffr. Theor. Gen. Crystallogr. **1976**, *32*, 751−767.
(56) Li, P.; Chen, I.-W.; Penner-Hahn, J. E. X-ray-absorption studies of zirconia polymorphs. I. Characteristic local structures. *Phys. Rev. B* **1993**, *48*, 10063.
(57) Gaultois, M. W.; Greedan, J. E.; Grosvenor, A. P. Investigation of coordination changes in substituted transition-metal oxides by K-edge XANES: Beyond the pre-edge. *J. Electron Spectrosc. Relat. Phenom.* **2011**, *184*, 192−195.
(58) Petkov, V. Pair distribution functions analysis. *Charact. Mater.* **2012**, 1361−1372.
(59) Masadeh, A. S. Total scattering atomic pair distribution function: new methodology for nanostructure determination. *J. Exp. Nanosci.* **2016**, *11*, 951−974.
(60) You, Y.; Manthiram, A. Progress in high-voltage cathode materials for rechargeable sodium-ion batteries. *Adv. Energy Mater.* **2018**, *8*, 1701785.
(61) Hwang, J. Y.; Kim, J.; Yu, T. Y.; Sun, Y. K. A new P2-type layered oxide cathode with extremely high energy density for sodium-ion batteries. *Adv. Energy Mater.* **2019**, *9*, 1803346.
(62) Han, Y.; Jung, S. H.; Kwak, H.; Jun, S.; Kwak, H. H.; Lee, J. H.; Hong, S. T.; Jung, Y. S. Single-or poly-crystalline Ni-rich layered cathode, sulfide or halide solid electrolyte: which will be the winners for all-solid-state batteries? *Adv. Energy Mater.* **2021**, *11*, 2100126.

https://doi.org/10.1021/acsenergylett.4c00490
ACS Energy Lett. 2024, 9, 2222−2230